IOP Publishing Smart Materials and Structures
Smart Mater. Struct. 32 (2023) 074001 (16pp) https://doi.org/10.1088/1361-665X/acd597

On-demand harmonic wave suppression in non-Hermitian space-time-periodic phased arrays

R Adlakha and M Nouh*

Department of Mechanical and Aerospace Engineering, University at Buffalo (SUNY), Buffalo, NY 14260-4400, United States of America

E-mail: mnouh@buffalo.edu

Received 15 February 2023, revised 21 April 2023
Accepted for publication 11 May 2023
Published 30 May 2023

Abstract

Phased arrays have been a cornerstone of non-destructive evaluation, sonar communications, and medical imaging for years. Conventional arrays work by imparting a static phase gradient across a set of transducers to steer a self-created wavefront in a desired direction. Most recently, space-time-periodic (STP) phased arrays have been explored in the context of multi-harmonic wave beaming. Owing to the STP phase profile, multiple scattered harmonics of a single-frequency input are generated which propagate simultaneously in different directional lanes. Each of these lanes is characterized by a principal angle and a distinct frequency signature that can be computationally predicted. However, owing to the Hermitian (real) nature of the spatiotemporal phase gradient, waves emergent from the array are still bound to propagate simultaneously along up- and down-converted directions with a perfectly symmetric energy distribution. Seeking to push this boundary, this paper presents a class of non-Hermitian STP phased arrays which exercise a degree of unprecedented control over the transmitted waves through an interplay between gain, loss, and coupling between its individual components. A complex phase profile under two special symmetries, parity-time (PT) and anti-PT, is introduced that enables the modulation of the amplitude of various harmonics and decouples up- and down-converted harmonics of the same order. We show that these arrays provide on-demand suppression of either up- or down-converted harmonics at an exceptional point—a degeneracy in the parameter space where the system's eigenvalues and eigenvectors coalesce. An experimental prototype of the non-Hermitian array is constructed to illustrate the selective directional suppression via time-transient measurements of the out-of-plane displacements of an elastic substrate via laser vibrometry. The theory of non-Hermitian phased arrays and their experimental realization unlock rich opportunities in precise elastoacoustic wave manipulation that can be tailored for a diverse range of engineering applications.

Supplementary material for this article is available online

Keywords: phased array, wave beaming, wave guidance, non-Hermitian

(Some figures may appear in colour only in the online journal)

* Author to whom any correspondence should be addressed.

1. Introduction

With the advancement in computing technology, parallel signal processors have become efficient and economical, and have led to the development of advanced phased arrays. Fundamentally, phased arrays consist of a set of wave-transmitting or receiving devices (transceivers) arranged in a specific geometrical pattern that allows efficient wave field control. They can achieve precise beam forming, steering, and focusing in their transmission mode and are capable of sensing waves that are incident on the array from a given direction in their reception mode [1]. Their working mechanism relies on constructive and destructive wavefront interferences induced by a prescribed (while transmitting) or inherent (while sensing) phase delay. Phased arrays can be geometrically classified into 1D linear arrays [2], 2D planar arrays [3], or 3D spherical arrays [4]. These could be further classified into uniform or non-uniform depending on the inter-element distance or pitch [5]. Owing to their versatility, they have found applications in RADAR [6], 5G communication [7–9], binaural audio synthesis [10, 11], home audio [12–14], ultrasound imaging [15, 16], structural health monitoring [17–24], acoustic levitation [25], and acoustic holography [26], to name a few.

The individual transducers of a conventional phased array are imposed with a static phase gradient which gives rise to their wave beaming ability. Lately, and inspired by recent progress in temporally-modulated phononic metamaterials, the notion of implementing a dynamic phase profile in a phased array, i.e. one that varies spatially along the length of the array but also simultaneously in time, has been shown to yield multiple beams which travel along different directions and within different frequency channels, representing small harmonic conversions of the fundamental and modulation frequencies [27, 28] (see figure 1(a)). These space-time-periodic (STP) arrays are described using Hermitian Hamiltonians, which represent the dynamics of energy-conservative systems that support real-valued energy spectra. Despite their appeal, the different beams generated in an STP array maintain perfect symmetry and possess identical energy amounts along the up- and down-converted paths [29]. In this work, we present the theoretical foundation and experimental realization of an STP phased array which breaks such symmetry and achieves on-demand suppression of a targetted harmonic by exploiting the non-Hermitian dynamics of the proposed system, as envisioned in figure 1(b).

Non-Hermitian Hamiltonians are used to depict the behavior of dissipative systems that exhibit complex-valued energy spectra. Bender and Boettcher showed that non-Hermitian systems which exhibit a special kind of symmetry, denoted parity-time (PT) symmetry, can have real-valued eigen spectra under certain conditions and be used to represent practical systems [30]. Simply put, this implies that hermiticity is not a necessary condition for a system to possess real-valued eigen spectra. PT-symmetric systems are unique in the sense that they are non-Hermitian systems with real-valued eigen spectra and show phase transition at exceptional points (EPs). EPs are degeneracies in the parameter space where two or more eigenvalues of the system coalesce. Numerous applications have been developed that exploit the nature of the system at an EP to observe intriguing wave phenomena such as unidirectional invisibility [31], enhanced sensing [32], asymmetric wave behavior in non-local metagratings [33], unidirectional excitation of surface plasmon polaritons [34], and polarization-sensitive optical field manipulation in metasurfaces [35]. Recently, Kawaguchi showed a non-reciprocal PT symmetry breakage in a lossy magneto-optical ring resonator coupled with a gain-loss ring resonator demonstrating a one-way EP [36]. In the elastic metamaterial community, Riva showed that a complex stiffness-modulated waveguide operates as a phononic filter in the unbroken PT-symmetric phase, but that as the modulation strength increases at the EP, the system shows asymmetric scattering capabilities [37]. Another effort by Moghaddaszadeh *et al* explored the wave dispersion characteristics of a 1D continuous rod with PT-symmetric STP elastic modulus [38]. As a counterpart to PT symmetry, Ge and Türeci introduced the anti-PT-symmetric system, which was achieved using a photonic structure with a coupled balanced positive and negative-index material [39]. Yang *et al* showed significant variation in the transport properties at the phase transition from anti-PT-symmetric to broken phase in a dissipatively coupled optical system [40]. Fan *et al* showed anti-PT symmetry in a fully passive nanophotonic platform consisting of coupled waveguides [41]. Intriguing phenomena such as power splitting, synchronized amplitude modulation, and phase-controlled dissipation have been explored by thermally tuning the nanophotonics platform at the phase transition point. Zhang *et al* showed synthetic phase transition from anti-PT symmetry to broken phase in a single optical microcavity [42].

By exploiting PT- and anti-PT-symmetric STP phase profiles, this work seeks to break the symmetric transmission of energy along the up- and down-converted harmonic channels of an STP phased array. The proposed class of non-Hermitian arrays maintains a degree of unprecedented control over the transmitted waves under the two special symmetries. The non-Hermitian phase profile enables the modulation of the amplitude of various harmonics and consequently, the decoupling of up- and down-converted harmonics of the same order, thus achieving on-demand suppression of either one at the system's EP. Following a comprehensive theoretical analysis, an experimental prototype of the non-Hermitian array is developed to illustrate the successful directional suppression via wave field measurements and reconstruction. Non-Hermitian STP phased arrays present an innovative approach to advancing acoustic communication systems. As will be shown here, the proposed array demonstrates the ability to communicate with multiple carriers at different frequencies, while being simultaneously capable of modulating the amplitude of specific directional channels to ensure appropriate communication strength or compensate for carriers (e.g. ships) at different proximity levels. Inversely, we envision the use of the same technology to identify the distance of a carrier based on signal strength. In what follows, we detail the theoretical foundation and experimental aspects of this class of non-Hermitian phased arrays.

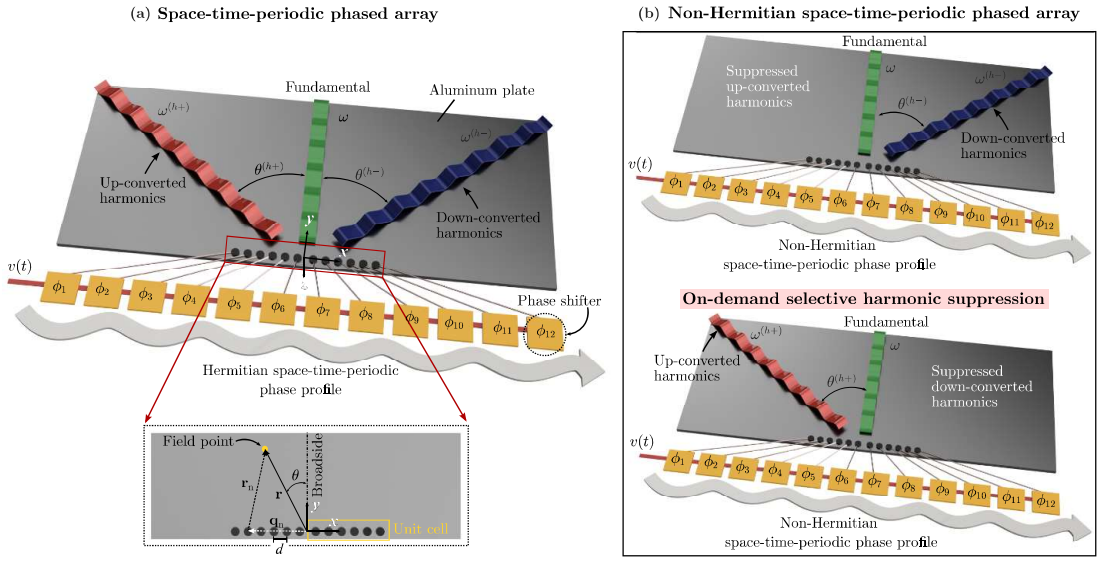

Figure 1. Conceptualization of a Hermitian vs a non-Hermitian space-time-periodic (STP) phased array. Both arrays are comprised of a set of transducers which are fed a space- and time-dependent voltage input via an equal set of phase shifters. (a) Hermitian STP phased array with fundamental, up-, and down-converted harmonics. The up- and down-converted harmonics show symmetric wave propagation about the broadside. (b) Non-Hermitian STP phased array with on-demand suppression of either the up- (*top*) or down-converted (*bottom*) harmonics.

2. Non-Hermitian phased arrays

We start by imposing a complex phase profile $_n$ i in a phased array, where and are the real and imaginary phase components. The complex nature of the profile introduces a gain-loss factor to the phase which manifests itself in the form of an amplification or decay of the amplitude of the supplied voltage to the nth transducer. Assuming a tonal input voltage signal to the nth phase shifter given by $v\ t$ $V_0 e^{i\ t}$, where is the frequency of excitation and V_0 is the amplitude, the phase shifted input voltage to the nth transducer can be derived as follows:

$$v_n\ t \quad v\ t\ e^{i\ _n} \quad V_0 e \quad e^{i\ t} \tag{1}$$

Here, the imaginary component of the phase profile, $_n$, controls the amplitude decay or amplification of the phase-shifted voltage signal while the real component, $_n$, controls the phase of the output voltage. In the following sections, we will analyze the behavior of a complex phase $_n$ showcasing PT and anti-PT symmetries by imposing certain conditions on and , which will be outlined.

2.1. PT-symmetric phased arrays

Mathematically, a PT-symmetric system is one that simultaneously shows parity: and time: symmetries, where is an arbitrary function of an argument , and denotes its complex conjugate. Since PT-symmetric systems represent a class of non-Hermitian systems, they are still complex valued, i.e. $_R$ i $_I$, where $_R$ and $_I$ are even and odd functions, respectively. A PT-STP phase profile refers to the implementation of PT symmetry in an STP phased array, which can be synthesized with periodic functions for the nth transducer in a phased array with N elements as follows:

$$_n \quad \cos\ _n \quad i\ \sin\ _n \tag{2}$$

where and denote the modulation depths for the real and imaginary periodic functions in the phase profile, and $_n$ $_m t$ $_m$ $\mathbf{q_n}$ is the space-time modulating argument where $_m$ is the temporal modulation frequency, $_m$ ^{3} is the spatial modulation frequency, and $\mathbf{q}_n$ ^{3} is the spatial location of the nth transducer. An expansion of equation (2) yields

$$_n \quad \frac{}{2} e^{i\ _n} \quad e^{\ i\ _n} \quad \frac{}{2} e^{i\ _n} \quad e^{\ i\ _n} \quad \frac{1}{2} \quad e^{i\ _n} \quad e^{\ i\ _n} \tag{3}$$

It can be seen from equation (3) that one term of the phase profile will vanish at certain values of the modulation depths (specifically, and). As will be shown later, this corresponds to full suppression of either an up- or down-converted harmonic of the beamed wave. In an STP phased array, the coupling of the space-time modulation with the exponential phase term gives rise to a series of up- and down-converted harmonics [29]. These harmonics can be computed by first expanding the input voltage to the nth transducer in equation (1) as follows:

$$v_n\ t \quad v\ t\ e^{\ i\ \cos\ _n} e^{\ i\ i\ \sin\ _n} \tag{4}$$

The real-valued exponent in the last term of equation (4) confirms that the imaginary component of the phase profile

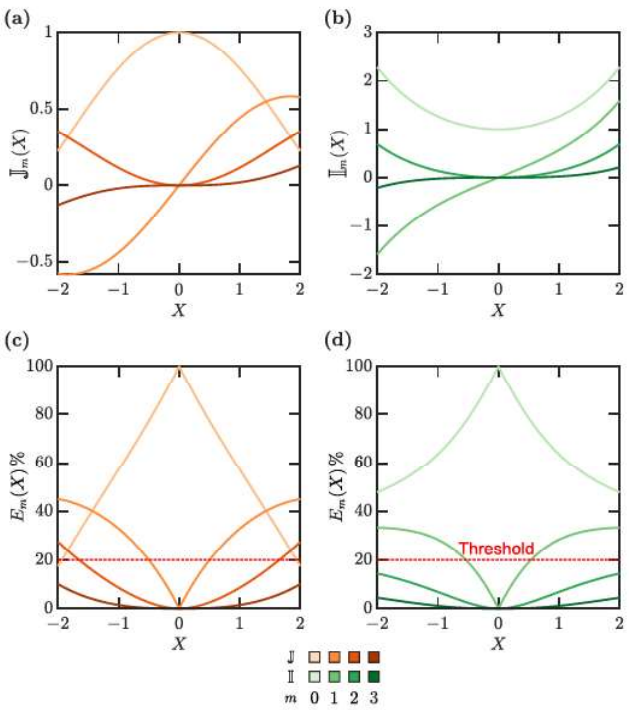

Figure 2. *Top*: Values of the mth order of the (a) Bessel $\mathbb{J}_m$ and (b) modified Bessel $\mathbb{I}_m$ functions of the first kind for an argument $X \in [-2,2]$. *Bottom*: Percentage energy E_m contained in the mth order of the (c) Bessel and (d) modified Bessel functions of the first kind for an argument $X \in [-2,2]$.

creates an amplitude, rather than a phase, variation; an observation which is consistent with equation (1). Using the Jacobi–Anger expansion, the voltage signal for the nth transducer can be expanded into a product of infinite Bessel functions via

$$e^{-i\delta\cos\xi_n} = \sum_{m=-\infty}^{\infty} (-i)^m \mathbb{J}_m(\delta) e^{im\xi_n} \tag{5a}$$

$$e^{-i(i\gamma)\sin\xi_n} = \sum_{m=-\infty}^{\infty} \mathbb{J}_m(-i\gamma) e^{im\xi_n} \tag{5b}$$

where $\mathbb{J}$ and $\mathbb{I}$ are the Bessel and modified Bessel functions, respectively. By defining the percentage energy concentrated in the mth order of the Bessel function as $E_m = \frac{|\mathbb{B}_m|}{\sum_{k=-2}^{2}|\mathbb{B}_m|} \times 100$ %, where $\mathbb{B} \in [\mathbb{J}, \mathbb{I}]$, limiting our analysis to the second order $\mathbb{J}$ and $\mathbb{I}$ functions ensures that no more than 20% of energy is concentrated in higher-order Bessel functions, as shown in figure 2, and constrains the values of the modulation depths to $\delta, \gamma \in [-2,2]$. Using equations (4) and (5), the expanded signal can therefore be described using a linear system which is given by

$$v_n(t) = v(t)\left[\mathbb{C}_{PT} \cdot \mathbb{E}^T(t)\right] \tag{6}$$

where $\mathbb{C}_{PT}$ and $\mathbb{E}$ are the amplitude and signal harmonic vectors, respectively. These vectors are defined as

$$\mathbb{C}_{PT} = \left[C_{PT}^{(2-)}\ iC_{PT}^{(1-)}\ C_{PT}^{(0)}\ iC_{PT}^{(1+)}\ C_{PT}^{(2+)}\right] \tag{7a}$$

Table 1. Amplitudes of various harmonics $\mathbb{C}_{PT}$ generated by the PT-symmetric phase profile as a function of $\mathbb{J}$, $\mathbb{I}$, δ, and γ.

Amplitude	Values
$C_{PT}^{(2-)}$	$\mathbb{J}_1(\delta)\mathbb{I}_1(\gamma) - \mathbb{J}_0(\delta)\mathbb{I}_2(\gamma) - \mathbb{J}_2(\delta)\mathbb{I}_0(\gamma)$
$C_{PT}^{(1-)}$	$-\mathbb{J}_1(\delta)\mathbb{I}_0(\gamma) + \mathbb{J}_0(\delta)\mathbb{I}_1(\gamma) + \mathbb{J}_1(\delta)\mathbb{I}_2(\gamma) + \mathbb{J}_2(\delta)\mathbb{I}_1(\gamma)$
$C_{PT}^{(0)}$	$\mathbb{J}_0(\delta)\mathbb{I}_0(\gamma) + 2\mathbb{J}_2(\delta)\mathbb{I}_2(\gamma)$
$C_{PT}^{(1+)}$	$-\mathbb{J}_1(\delta)\mathbb{I}_0(\gamma) - \mathbb{J}_0(\delta)\mathbb{I}_1(\gamma) + \mathbb{J}_1(\delta)\mathbb{I}_2(\gamma) - \mathbb{J}_2(\delta)\mathbb{I}_1(\gamma)$
$C_{PT}^{(2+)}$	$-\mathbb{J}_1(\delta)\mathbb{I}_1(\gamma) - \mathbb{J}_0(\delta)\mathbb{I}_2(\gamma) - \mathbb{J}_2(\delta)\mathbb{I}_0(\gamma)$

$$\mathbb{E} = [\Xi^{(2-)}\ \Xi^{(1-)}\ \Xi^{(0)}\ \Xi^{(1+)}\ \Xi^{(2+)}]. \tag{7b}$$

The amplitude values $C_{PT}^{(h)}$, where $h \in [-2,2]$, are defined in table 1 such that for example $h = 1$ and $h = -1$ denote the first up- and down-converted harmonics, respectively, $h = 2$ and $h = -2$ denote the second up- and down-converted harmonics, respectively, and so forth. $\Xi^{(h)}$ is defined as $e^{ih(\omega_m t - \kappa_m q_n)}$. A complete derivation of these coefficients is provided in the supplementary material.

2.2. Anti-PT-symmetric phased arrays

Non-Hermitian systems that show space-time reflection antisymmetry are referred to as anti-PT-symmetric systems. Mathematically, a system represented by $\mathcal{X}(\eta) = \mathcal{X}_R(\eta) + i\mathcal{X}_I(\eta)$ is considered anti-PT symmetric if it obeys $\mathcal{X}^*(-\eta) = -\mathcal{X}(\eta)$. This can be achieved by setting the $\mathcal{X}_R(\eta)$ and $\mathcal{X}_I(\eta)$ as odd and even functions, respectively. An anti-PT phase profile in an STP phased array (or APT-STP phase profile) with periodic functions for the nth transducer in a phased array with N elements can be synthesized as follows:

$$\psi_n(\alpha,\beta) = \alpha\sin(\xi_n) + i\beta\cos(\xi_n) \tag{8}$$

where α and β denote the modulation depths for the real and imaginary components of the APT-STP phase profile. Similar to the expansion shown in equation (3), equation (8) can be expanded as follows:

$$\begin{aligned}\psi_n(\alpha,\beta) &= -\frac{i\alpha}{2}\left[e^{i\xi_n} - e^{-i\xi_n}\right] + \frac{i\beta}{2}\left[e^{i\xi_n} + e^{-i\xi_n}\right] \\ &= -\frac{i}{2}\left[(\alpha-\beta)e^{i\xi_n} - (\alpha+\beta)e^{-i\xi_n}\right]\end{aligned} \tag{9}$$

and used to selectively suppress up or down-converted harmonics, when $\alpha = \beta$ and $\alpha = -\beta$, respectively.

Similar to the PT-STP case, a series of harmonics are generated by applying an APT-STP phase profile to an input voltage $v(t)$. The phase-shifted voltage signal for the nth transducer is defined as

$$v_n(t) = v(t)e^{-i\alpha\sin\xi_n}e^{-i(i\gamma)\cos\xi_n}. \tag{10}$$

Following the Jacobi–Anger expansion, the phase-shifted voltage signal at the nth transducer can be expanded into a series of harmonics using the following relations:

$$e^{-i\alpha\sin(\xi_n)} = \sum_{m=-\infty}^{\infty} \mathbb{J}_m(-\alpha)e^{i\xi_n} \tag{11a}$$

Table 2. Amplitudes of various harmonics $\mathbb{C}_{\text{APT}}$ generated by the anti-PT-symmetric phase profile as a function $\mathbb{J}$, $\mathbb{I}$, α, and β.

Amplitude	Values
$C_{\text{APT}}^{(2-)}$	$\mathbb{J}_1(\alpha)\mathbb{I}_1(\beta)+\mathbb{J}_0(\alpha)\mathbb{I}_2(\beta)+\mathbb{J}_2(\alpha)\mathbb{I}_0(\beta)$
$C_{\text{APT}}^{(1-)}$	$\mathbb{J}_1(\alpha)\mathbb{I}_0(\beta)+\mathbb{J}_0(\alpha)\mathbb{I}_1(\beta)-\mathbb{J}_1(\alpha)\mathbb{I}_2(\beta)+\mathbb{J}_2(\alpha)\mathbb{I}_1(\beta)$
$C_{\text{APT}}^{(0)}$	$\mathbb{J}_0(\alpha)\mathbb{I}_0(\beta)+2\mathbb{J}_2(\alpha)\mathbb{I}_2(\beta)$
$C_{\text{APT}}^{(1+)}$	$-\mathbb{J}_1(\alpha)\mathbb{I}_0(\beta)+\mathbb{J}_0(\alpha)\mathbb{I}_1(\beta)+\mathbb{J}_1(\alpha)\mathbb{I}_2(\beta)+\mathbb{J}_2(\alpha)\mathbb{I}_1(\beta)$
$C_{\text{APT}}^{(2+)}$	$-\mathbb{J}_1(\alpha)\mathbb{I}_1(\beta)+\mathbb{J}_0(\alpha)\mathbb{I}_2(\beta)+\mathbb{J}_2(\alpha)\mathbb{I}_0(\beta)$

$$e^{-i(i\beta)\cos(\xi_n)}=\sum_{m=-\infty}^{\infty}\mathbb{J}_m(-i\beta)e^{i\xi_n} \tag{11b}$$

and the analysis is again limited to the second order $\mathbb{J}$ and $\mathbb{I}$ functions. Here, the expanded signal can be described using a linear system which is given by

$$v_n(t)=v(t)\left[\mathbb{C}_{\text{APT}}\cdot\mathbb{E}^T(t)\right] \tag{12}$$

where $\mathbb{C}_{\text{APT}}$ and $\mathbb{E}$ are the amplitude and signal harmonic vectors, respectively. These vectors are defined as

$$\mathbb{C}_{\text{APT}}=[C_{\text{APT}}^{(2-)}\ C_{\text{APT}}^{(1-)}\ C_{\text{APT}}^{(0)}\ C_{\text{APT}}^{(1+)}\ C_{\text{APT}}^{(2+)}] \tag{13a}$$

$$\mathbb{E}=[\Xi^{(2-)}\ \Xi^{(1-)}\ \Xi^{(0)}\ \Xi^{(1+)}\ \Xi^{(2+)}]. \tag{13b}$$

The amplitude values $C_{\text{APT}}^{(h)}$, where $h\in[-2,2]$, are defined in table 2. A complete derivation of these coefficients is provided in the supplementary material. In the remainder of the manuscript, the subscripts $(\bullet)_{\text{PT}}$ and $(\bullet)_{\text{APT}}$ are omitted for brevity.

2.3. Energy analysis of various harmonics

The amplitude and energy of various harmonic orders (h-Order) is a nonlinear function of the two modulation depths, namely (δ,γ) for PT-symmetric and (α,β) for anti-PT-symmetric systems. The ratio of these two modulation depths to one another plays a significant role in controlling the amplitude of the various harmonics and allows for the transition into different phases of PT- and anti-PT symmetry, which will be detailed next. This γ/δ ratio for the PT-symmetric case and β/α for the anti-PT-symmetric one is henceforth defined as the hermiticity ratio. By tuning the hermiticity ratio, the amplitude and consequently the energy of various harmonics can be varied.

Figure 3(a) depicts the variation in the amplitudes $C^{(h)}$ and percentage energy $E^{(h)}$ for $h\in[-2,2]$ for different values of $\delta\in[-2,2]$ for an STP phased array with a PT-symmetric phase profile, where $E^{(h)}$ is defined as follows:

$$E^{(h)}=\frac{|C^{(h)}|}{\sum_{k=-2}^{2}|C^{(k)}|}\times 100\ \%. \tag{14}$$

This is displayed for the following hermiticity ratios: $-1.5,-1,-0.5,0,0.5,1$, and 1.5. Figure 3(b) shows the corresponding behavior of an STP phased array with an anti-PT-symmetric phase profile for different values of $\alpha\in[-2,2]$. It can be observed that all down-converted harmonics are suppressed when the hermiticity ratio hits unity ($\gamma/\delta=1$) for the PT-symmetric system, while the same behavior takes place when the hermiticity ratio hits negative unity ($\beta/\alpha=-1$) for the anti-PT-symmetric system. On the other hand, up-converted harmonic suppression is achieved when $\gamma/\delta=-1$ and $\beta/\alpha=1$. In figure 3, the backgrounds for these two scenarios are uniquely shaded for convenience. The ability to selectively suppress up- or down-converted harmonics is central to the non-Hermitian phased array. The special values of the hermiticity ratio at which this happens correspond to what is known as EPs for the PT- and anti-PT-symmetric systems, which will be discussed in the next section. As a control test, the energy contained in up- and down-converted harmonics of various orders is identical when the hermiticity ratio is zero, indicating the lack of dissipation and the return of the system to a Hermitian state. The amplitude of the fundamental harmonic ($h=0$) is a non-linear function of the zeroth and second order Bessel $\mathbb{J}$ and modified Bessel $\mathbb{I}$. It is important to note that, for the selected values of $\delta,\alpha\in[-2,2]$, this amplitude never reaches zero regardless of the hermiticity ratio, in both the PT- and anti-PT-symmetric cases. Consequently, the fundamental harmonic is never suppressed, and $E^{(0)}\%$ is always greater than zero.

3. Eigen spectra analysis

Contrary to non-dissipative systems that are described by Hermitian Hamiltonians which exhibit real eigen spectra, dissipative systems are typically associated with non-Hermitian Hamiltonians which exhibit complex eigen spectra that depict the non-conservative behavior of the system. Interestingly, dissipative systems that show PT or anti-PT symmetry have been shown to support real eigen spectra for a specific range of modulation depth values. Both PT- and anti-PT-symmetric systems show a phase transition from an exact phase to a broken phase at the EP. The EP is defined as a degeneracy in the parameter space for which two or more eigenvalues of the system coalesce [43]. The eigen spectra of a PT-symmetric system support real values in the PT exact phase. The EP occurs when the hermiticity reaches unity and the eigenvalues coalesce. Past the EP, the PT-symmetric system exhibits complex eigen spectra. The exact opposite scenario takes place in the case of an anti-PT-symmetric system.

The scattering matrix of an STP phased array can be utilized to depict the system's eigen spectra and illustrate the various phase transitions. In the array's transmission mode, the scattering matrix $\mathbb{S}$ can be obtained from $\mathbf{V}_{\text{out}}=\mathbb{S}\mathbb{E}^T v$ for both PT- and anti-PT-symmetric systems, with $\mathbf{V}_{\text{out}}$ being a vector of the various harmonics in the output voltage signal. The scattering matrix can be defined as follows [27]:

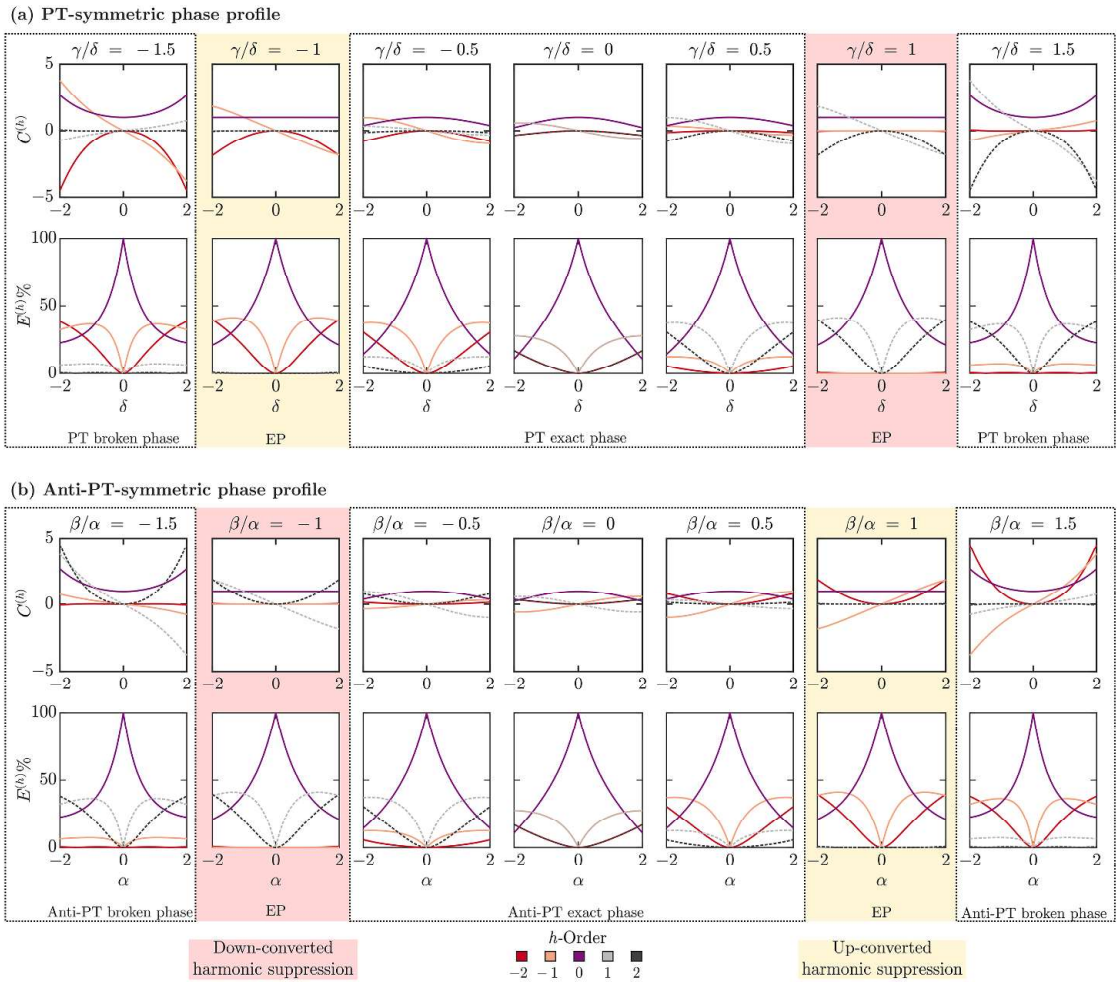

Figure 3. The amplitude C^h and percentage energy E^h of the hth harmonic for (a) a PT-symmetric phase profile and (b) an anti-PT-symmetric phase profile. The different harmonics in each subplot are color coded to reflect the value of h. The yellow-shaded scenarios depict a suppression of the up-converted harmonic when the hermiticity ratio is equal to 1 for the PT-symmetric system and 1 for the anti-PT-symmetric one. The pink-shaded scenarios depict a suppression of the down-converted harmonic when the hermiticity ratio is equal to 1 for the PT-symmetric system and 1 for the anti-PT-symmetric one.

$$\begin{matrix} C^0 & C^1 & C^2 & 0 & 0 \\ C^1 & C^0 & C^1 & C^2 & 0 \\ C^2 & C^1 & C^0 & C^1 & C^2 \\ 0 & C^2 & C^1 & C^0 & C^1 \\ 0 & 0 & C^2 & C^1 & C^0 \end{matrix} \tag{15}$$

This matrix represents a fifth-order system which yields a higher odd-order EP, where one eigenvalue always remains real and the other four diverge in the complex domain as shown in figure 4. All the eigenvalues coalesce at 1 for the PT-symmetric system and 1 for the anti-PT-symmetric system, enabling the transition from the exact to the broken phase at the EP. Figures 4(a) and (c) display the real component of the eigen spectra for the PT-symmetric and anti-PT-symmetric systems, respectively, while figures 4(b) and (d) display the imaginary component of the eigen spectra for a hermiticity ratio ranging between 0 and 2. The plots are evaluated at 1 35 and 1 35, respectively. In figure 4(d), a second EP can be observed which is a feature of higher-order Hamiltonians [44, 45], but is not a focus of this work.

4. Optimal modulation depths of maximizing hth order non-suppressed harmonic

As eluded to in section 2, complete suppression of up- or down-converted harmonics can be achieved at the EP for various modulation depths. Additionally, the energy contained in the various non-suppressed harmonics can be tuned by controlling the same. Since the absolute value of the hermiticity ratio is equal to one at the EP, controlling the real component of the modulation depth only, i.e. for PT-symmetric and for anti-PT-symmetric systems, is sufficient. Due to the nonlinear relation between the energy of the non-suppressed harmonics on one hand, and or at the EP on the other, a nonlinear optimization problem can be formulated in order to find the optimal modulation depths needed to maximize the hth

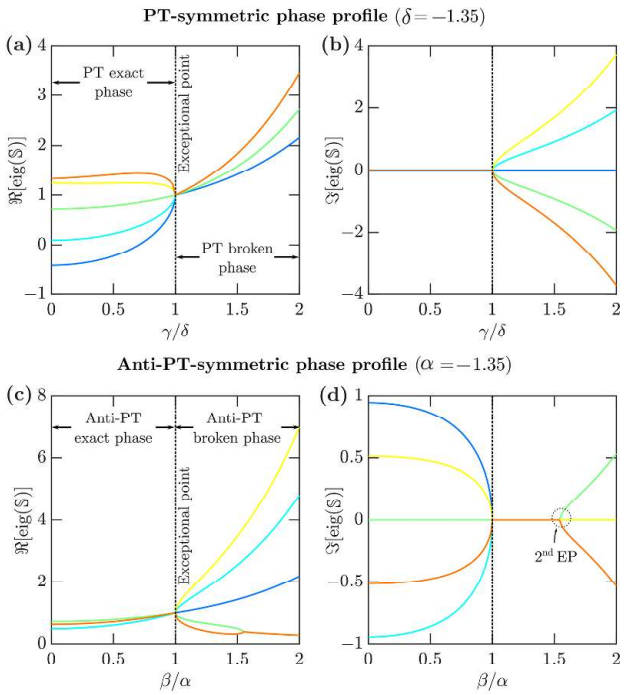

Figure 4. Eigen spectra of the scattering matrix of the 5th order. (a), (b) show the real and imaginary components of the eigen spectra for a PT-symmetric phase profile and a varying hermiticity ratio 2 2 with 1 35. (c), (d) show the real and imaginary components of the eigen spectra for an anti-PT-symmetric phase profile and a varying hermiticity ratio 2 2 with 1 35. The dashed black line shows the exceptional point (EP) at 1.

non-suppressed harmonic. The optimization problem can be described as

$$\begin{aligned} \max J \quad & \frac{E^{h}}{\sum_{k}^{2} {}_{2}E^{k}} \\ \text{s.t.} \quad & \text{or} \quad 1 \ 1 \\ & \text{or} \quad 2 \ 2 \\ & 0 \quad 0 \end{aligned} \tag{16}$$

and can be solved using any established optimization algorithm (Here, `fmincon` in MATLAB's optimization toolbox was utilized). Additional constraints can be added to the optimization problem to control the energy of other non-suppressed harmonic orders. Figures 5(a) and (b) show the amount of energy contained in different harmonic orders for 1 5 1 5 for the down-converted (1) and up-converted harmonic suppression (1) cases for a PT-symmetric phase profile. Similarly, figures 5(c) and (d) show the amount of energy contained in different harmonic orders for 1 5 1 5 for the down-converted (1) and up-converted harmonic suppression (1) cases for an anti-PT-symmetric phase profile. For a complete suppression of all down-converted harmonics and a maximization of the first up-converted harmonic (h 1), the optimization algorithm yields modulation depths values of 1 35 1 35 for the PT-symmetric phase profile and 1 35 1 35 for the anti-PT-symmetric phase profile. Similarly, for a complete suppression of all up-converted harmonics and a maximization of the first down-converted harmonic (h 1), the optimal modulation depths are found to be 1 35 1 35 and 1 35 1 35 for the PT- and anti-PT-symmetric systems, respectively. Finally, figures 5(e) and (f) show the percentage energy in the different harmonics at the optimal modulation depths for aforementioned scenarios.

5. Wave field derivation and analysis

In order to depict the suppressed harmonics in the wave beaming patterns of the non-Hermitian phased array, an expression for the wave field generated by the various harmonics due to an input voltage signal needs to be derived. Here, we utilize a phased array which is comprised of a series of piezoelectric transducers bonded to an elastic medium (see figure 1).

5.1. Wave field generated by a single piezoelectric transducer

The input voltage signal to the nth transducer is augmented with a static phase gradient $_{c}$ ^{3} to allow for the steering of the various wave harmonics as shown below:

$$v_n\ t \quad v\ t\ \mathrm{e}^{\ \mathrm{i}\ _{c}\mathbf{q}_n \qquad T} \tag{17}$$

It should be noted that the PT- or anti-PT-symmetric nature of the system arises from the complex-valued portion of the STP phase profile, and that the inclusion of an additional static phase gradient $_{c}$ does not alter this nature. Incorporating $_{c}$ introduces an additional degree of tunability by enabling us to adjust the direction of the array's broadside.

Considering a tonal input signal $v\ t \quad V_0\mathrm{e}^{\mathrm{i}\ t}$, the voltage signal for the nth transducer can be further expanded into harmonic components as follows:

$$v_n^{h}\ t \quad V_0\ _{h}\mathrm{e}^{\mathrm{i}\ t \quad _{c}\mathbf{q}_n \qquad h} \tag{18}$$

where $_{h}$ is the element of the amplitude matrix representing the amplitude of the hth harmonic. The frequency (, $_{m}$) and phase gradient ($_{c}$, $_{m}$) terms can be grouped as follows:

$$v_n^{h}\ t \quad V_0\ _{h}\mathrm{e}^{\mathrm{i}\ \ h\ _{m}\ t \quad _{c}\ h\ _{m}\ \mathbf{q}_n} \tag{19}$$

which can be simplified to

$$v_n^{h}\ t \quad V_0\ _{h}\mathrm{e}^{\mathrm{i}\ \ ^{h}\ t \quad _{c}^{h}\mathbf{q}_n} \tag{20}$$

where the ^{h} denotes a frequency shift such that ^{h} $h\ _{m}$ is the frequency of the hth harmonic, while ^{h} denotes a phase gradient shift as $_{c}^{h}$ $_{c}\ h\ _{m}$. So for example, the first up- and down-converted harmonics would be represented by ^{1} $_{m}$ and ^{1} $_{m}$, respectively, in the frequency domain, while their phase gradients would be represented by $_{c}^{1}$ $_{c}\ _{m}$ and $_{c}^{1}$ $_{c}\ _{m}$, respectively. Lastly, the input voltage to the nth transducer is computed as $v_n\ t \quad \sum_{k}^{2} {}_{2}v_n^{k}\ t$.

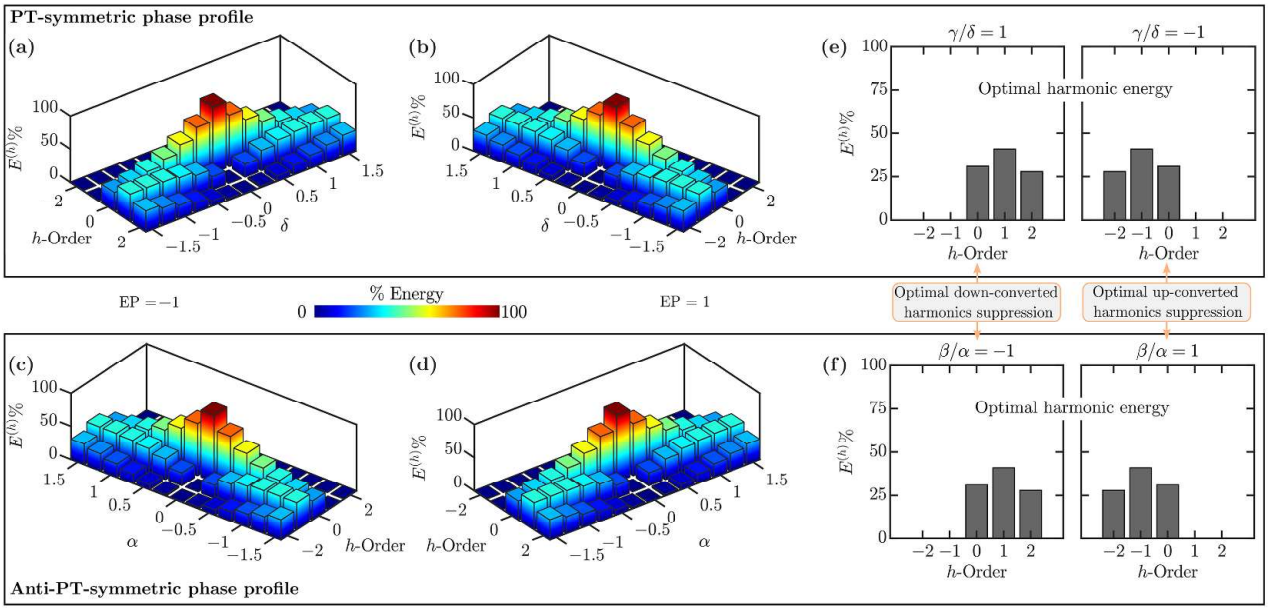

Figure 5. Percentage energy E ^{h} contained in the hth harmonic for a PT-symmetric phase profile (*top*) and an anti-PT-symmetric phase profile (*bottom*). (a), (b) are evaluated using 1 5 1 5 . (c), (d) are evaluated using 1 5 1 5 . (e) and (f) show the energy of different harmonics at the optimal modulation depths needed to maximize the first up/down-converted harmonic in the PT- and anti-PT-symmetric systems, respectively.

In an elastic phased array, the nth piezoelectric transducer excites various modes of symmetric and anti-symmetric Lamb waves in an elastic medium. Higher-order symmetric and anti-symmetric Lamb waves can be neglected since the excitation frequency is sufficiently low, thus only inducing the fundamental symmetric S_0 and antisymmetric A_0 modes [46]. The latter can be approximated as extensional and flexural waves, respectively, for a sufficiently small h ^{h} 2 100 kHz mm, where h is the thickness of the elastic substrate [29]. We henceforth focus on anti-symmetric Lamb waves generated by the phased array since they represent the most dominant waves under 100 kHz [47] and to facilitate our experimental measurements using out-of-plane laser Doppler vibrometry, as will be detailed in section 7. To ensure that the correct out-of-plane wave modes are excited, the excitation piezoelectric transducers are attached to only one face of the elastic substrate in both the FE simulations and the experimental apparatus. This is discussed in detail in the supplementary section. Under the aforementioned assumption, the hth order anti-symmetric Lamb waves $_{n}^{h}$ **r** t generated by the nth transducer can be modeled as follows:

$$_{n}^{h}\mathbf{r}\,t \quad \frac{V_0\ {}_{h}B^{h}}{\mathbf{r}_n\ ^{1\ 2}}\mathrm{e}^{\mathrm{i}\ {}^{h}t\ {}_{a}^{h}\mathbf{r}_n}\mathrm{e}^{\ \mathrm{i}\ {}_{c}^{h}\mathbf{q}_n} \quad \frac{V_0\ {}_{h}B^{h}}{\mathbf{r}_n\ ^{1\ 2}}\mathrm{e}^{\mathrm{i}\ {}^{h}t\ {}_{a}^{h}\mathbf{r}}\mathrm{e}^{\mathrm{i}\ {}_{c}^{h}\ {}_{c}^{h}\mathbf{q}_n} \tag{21}$$

where the wavenumber for the hth order anti-symmetric Lamb wave is defined as $_{a}^{h}$ $_{a}^{h}$ $\overline{{}^{h}}$ 12 1 ^{2} $Eh^{2\ 1\ 4}$ s.t. $_{a}^{h}$ ^{3} with E, , and denoting the elastic modulus, density, and Poisson's ratio of the medium, respectively. Additionally, **r** ^{3} is the position vector of an arbitrary field point and $\mathbf{r}_n$ **r** $\mathbf{q}_n$ ^{3} is the relative position vector between the field point and the nth transducer. Lastly, the hth order anti-symmetric Lamb wave coefficient is defined as

$$B^{h} \quad \overline{2}\mathrm{e} \quad {}^{4}B_{a}^{h} \quad \overline{{}_{a}^{h}} \tag{22}$$

As it is evident from the mathematical development in this section, the nth transducer excites waves with different harmonics in both frequency and wavenumber space which could be summed to yield the net wave field generated by the nth piezoelectric transducer $_{n}\mathbf{r}\,t$ $_{k\ 2}^{2}$ $_{n}^{k}\mathbf{r}\,t$.

5.2. Aggregate wave field generated by the phased array

Wave beaming is achieved as a consequence of constructive and destructive interferences of the wave fields generated by the N piezoelectric transducers in the phased array. An expression for the aggregate wave field generated by the phased array is derived by summing up the individual wave fields of the N transducers as follows:

$$^{h}\mathbf{r}\,t \quad \sum_{n\ 1}^{N} {}_{n}^{h}\mathbf{r}\,t \quad V_0\ {}_{h}B^{h}\mathrm{e}^{\mathrm{i}\ {}^{h}t\ {}_{a}^{h}\mathbf{r}} \sum_{n\ 1}^{N} \frac{\mathrm{e}^{\mathrm{i}\ {}_{a}^{h}\ {}_{c}^{h}\mathbf{q}_n}}{\mathbf{r}_n\ ^{1\ 2}} \tag{23}$$

Given the uniform linear configuration of the array (centered around the y-axis in figure 1), the location of

the nth transducer can be written as $\mathbf{q}_n \quad x_n \; 0 \; 0^T$ and the spatial modulation frequency as $\quad \quad 0 \; 0^T$. As such, equation (23) can be simplified to

$$\mathbf{r}\,t \quad V_0 \; B \; \mathrm{e}^{\mathrm{i}\,t} \; \mathbf{r} \; \sum_{n=1}^{N} \frac{\mathrm{e}^{\mathrm{i}\, \sin \; x_n}}{\mathbf{r}_n^{1\,2}} \tag{24}$$

where $\;$ is the direction of the hth harmonic wave with respect to the broadside. Lastly, the net harmonic wave fields generated by the phased array are summed to yield the net displacement field as $\mathbf{r}\,t \quad \sum_{k=2}^{2} \mathbf{r}\,t$.

5.3. Direction of the hth order harmonic wave

An STP phased array is capable of beaming different harmonics in their respective directions. The principal transmission direction $\;$ of a given harmonic h is found when the maximum wave amplitude is achieved in equation (24), i.e. when the argument of the summation exponential term approaches zero which yields

$$\quad \sin^{-1} \left(\frac{\quad}{\quad} \right) \tag{25}$$

As can be inferred from equation (25), it is worth noting that the direction of the hth harmonic is dependent on the phased array parameters $\;$, $\;$, and $\;$. Therefore, for desired harmonic directions, the phased array parameters can be easily computed, thus enabling the inverse problem.

6. Full wave simulations

Finite element (FE) simulations are conducted on a thin-circular Aluminum plate (5052 Aluminum Alloy) of h 1 27 mm thickness and 8 m radius. A phased array comprised of 12 piezoelectric transducers is synthesized by using circular edge sources of radius 5 mm. Each edge source is excited with individually modulated signals with an excitation frequency of 2 3 kHz, modulation frequency $\quad$ 2 0 05 kHz, static phase gradient $\quad$ 0 rad m^{-1}, and modulation spatial frequency $\quad$ 20 rad m^{-1}. Due to the periodicity of the phase profile, every 6 piezoelectric transducers compose one spatial unit cell with a modulation traveling velocity of $\quad$ 5 m s^{-1}. The duration of each simulation is 20 ms to ensure an adequate frequency resolution is maintained while computing the frequency spectrum and to minimize the effect of boundary reflections. The FE model is divided into two regions: An 8 m semicircular domain (to avoid reflections) and a 1 07 0 53 m^2 rectangular domain (to match the experimental apparatus), both made up of triangular elements which are sufficiently smaller than the wavelength. Figure 6(a) shows the wave field generated by the non-Hermitian phased array for the optimal up-converted harmonic suppression (left) and down-converted harmonic suppression (right) cases at their respective modulation depths in the PT-symmetric system. Figure 6(b) shows the direction of various harmonic components using a fast Fourier transform (FFT) of all points in space while isolating the different frequency components for optimal visualization.

The directional behavior of the various harmonics and their frequency content corresponding to an up-converted harmonic suppression is shown in the wave fields of the top row of figure 6(b) ranging from h 2 (2 2 2 90 kHz) to h 2 (2 2 3 10 kHz). The two rightmost subplots validate the suppression efficiency and confirm the lack of any noticeable propagation of up-converted frequencies. Further, it can be noted that the magnitude of the first down-converted harmonic wave is maximum as seen at 2.95 kHz, thereby validating the theoretical analysis presented in section 4 for the optimal modulation depths. For the propagating modes, the principal direction is ^{0} 0 for the fundamental mode, ^{1} 0 22 rad for the first down-converted harmonic, and ^{2} 0 50 0 22 i rad for the second down-converted harmonic. The complex value of the second down-converted harmonic direction indicates an evanescent mode which is directed towards the end-fire direction for the prescribed phased array parameters (2 3 00 kHz, $_m$ 2 0 05 kHz, $_c$ 0 rad m^{-1}, and $_m$ 20 rad m^{-1}). Similarly, the bottom row of figure 6(b) validates the down-converted harmonic suppression showing negligible magnitudes at 2.90 and 2.95 kHz. Additionally, the magnitude of the first up-converted harmonic is maximum as seen at 3.05 kHz. For the propagating modes, the principal directions are ^{0} 0, ^{1} 0 23 rad, and ^{2} 0 50 0 24 rad, indicating an evanescent mode for the second up-converted harmonic. Although these evanescent modes are visible close to the end-fire direction in the FE simulations due to the presence of amplified side lobes, these waves are generally not visible in an experiment setting.

It is important to note that FE simulations of the anti-PT-symmetric phased array yields the exact same results shown in figure 6. This is expected since the energy of different wave harmonics is identical whether the suppression is caused by PT- and anti-PT-symmetric phase profiles, as confirmed earlier in figure 3. However, a comparison of equations (7) and (13) suggests that a phase difference of 2 rad exists between the first non-suppressed harmonics of the PT- and the anti-PT-symmetric cases. Figure 7 displays the difference between the PT-symmetric and anti-PT-symmetric FFT phase angle of the dominant frequency of the temporal signals, denoted $_{PT}$ $_{APT}$, captured at the circular marker locations in figure 6 for both the fundamental and the first non-suppressed harmonic directions. For example, figure 7(a) shows the aforementioned difference in the up-converted harmonic suppression scenario and shows that while the fundamental frequency exhibits approximately zero phase difference between the PT- and anti-PT-symmetric systems, the first down-converted harmonic ^{1} exhibits a phase shift of approximately 2 rad as theoretically predicted. Figure 7(b) confirms the same observation in the down-converted harmonic suppression scenario.

7. Experimental apparatus and results

To validate the derived theoretical framework for on-demand selective harmonic wave suppression, an experimental

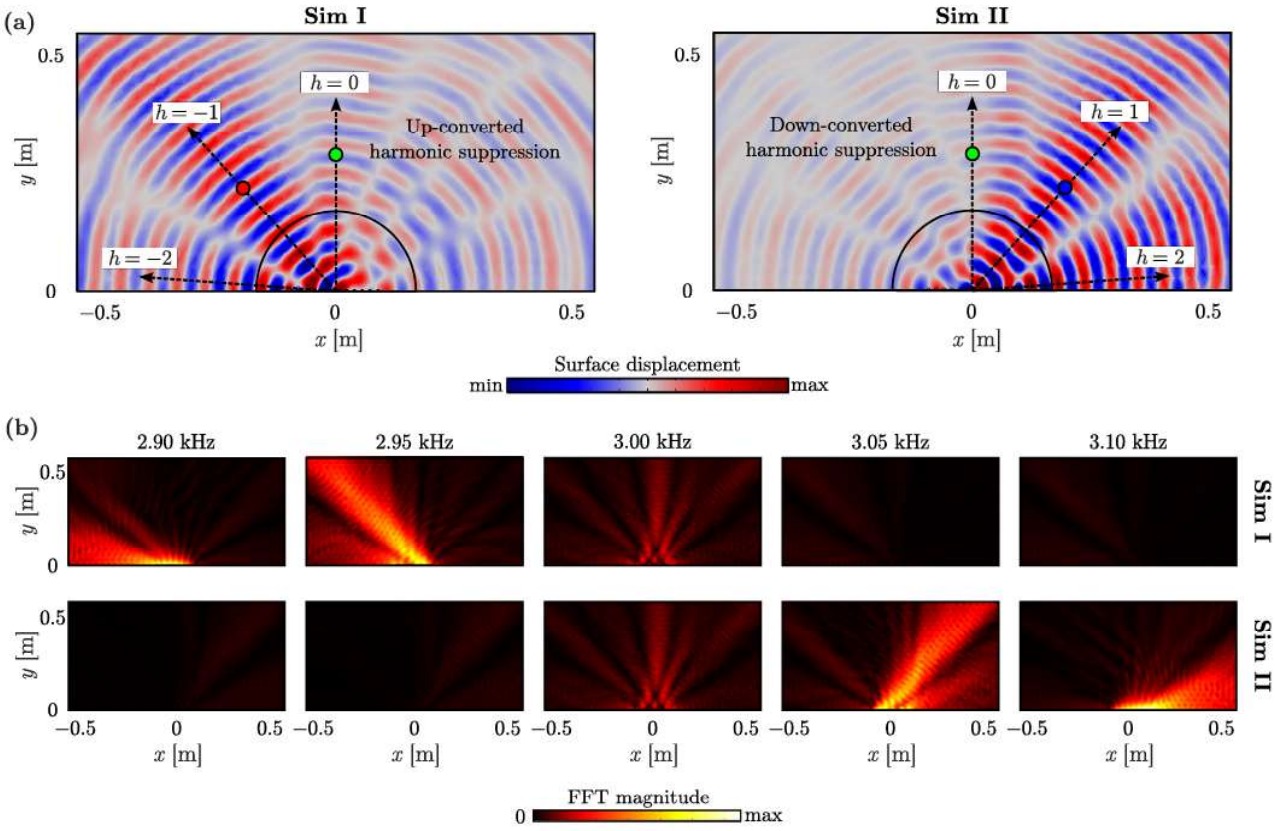

Figure 6. (a) Full wave (displacement) field of a non-Hermitian STP phased array with a PT-symmetric phase profile at $t = 3$ ms corresponding to an up-converted harmonic suppression (Sim (I) and a down-converted harmonic suppression (Sim II). Markers indicate sensors at a radius of 0.3 m from the center that capture time-domain signals at the depicted points in the wave field corresponding to the fundamental (green), up-converted (blue), and down-converted (red) directions. (b) FFT magnitudes for the various harmonics within the up-converted harmonic suppression case (top row) and down-converted harmonic suppression case (bottom row).

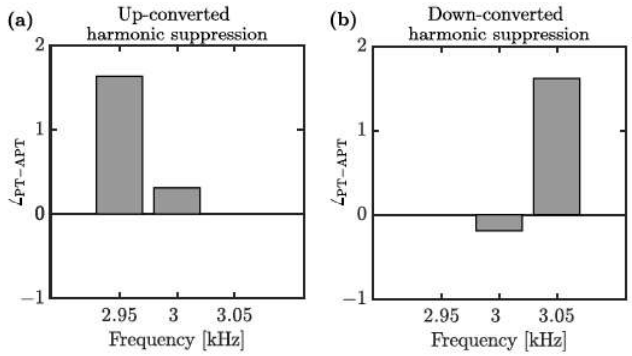

Figure 7. Difference between the PT-symmetric and anti-PT-symmetric FFT phase angle of the dominant frequency of the temporal signals, denoted $\angle_{\text{PT APT}}$, captured at the circular marker locations in figure 6 for both the fundamental (green marker) and the first non-suppressed harmonic direction. The latter is the first down-converted harmonic (red marker) in (a) and the first up-converted harmonic (blue marker) in (b). The figure shows that while the fundamental frequency exhibits approximately zero phase difference between the PT- and anti-PT-symmetric systems, the first non-suppressed harmonic whether in (a) or (b) exhibits a phase shift of approximately $\pi/2$ as theoretically predicted.

apparatus was constructed consisting of an Aluminum plate and a piezoelectric STP phased array. The phased array consists of twelve piezoelectric transducers (Manufacturer: Steminc Inc. Model: SMD05T04R111WL) that form two spatial units. These transducers produce the required anti-symmetric Lamb waves by inducing in-plane radial strain when excited. The piezoelectric transducers are individually controlled with voltage signals, as shown in figure 8. Due to the inherent periodicity, the number of individual signals required is reduced to six which contain the space-time-varying phase

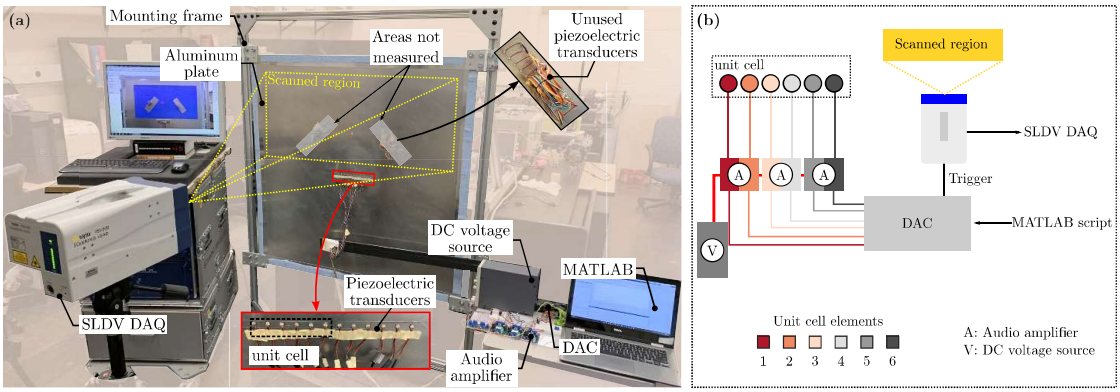

Figure 8. Overview of the experiment setup of a non-Hermitian STP phased array. (a) Entire experimental apparatus used to characterize the performance of the non-Hermitian array. 12 Piezoelectric transducers are bonded to an elastic medium in the form of an aluminum plate. A scanning laser Doppler vibrometer (SLDV) is used to capture the wave field via out-of-plane displacement measurements. A MATLAB script is used to generate the excitation signals and an audio digital-to-analog converter (DAC) transorms the digital excitation to an analog domain, which is amplified prior to being fed to the piezoelectric transducers. (b) Schematic diagram of the circuit used to drive the various piezoelectric transducers and to trigger the SLDV measurements.

profile. The transducers are epoxy-bonded (Manufacturer: 3M, Model: Scotch-Weld DP 270) to the center of an Aluminum plate (5052 Aluminum Alloy) which has a side length of 1.07 m and a thickness of 1.27 mm. For a complete description of the experiment apparatus, the reader is directed to [29], where a similar setup was used to demonstrate the operational concept of a nonreciprocal elastic phased array.

The six-channel phase-shifted signals, shown in figures 9 and 10, are digitally created using a custom MATLAB script that incorporates the non-Hermitian phase shift requirements. These digital signals are converted to the analog domain using an audio digital-to-analog converter which communicates with the MATLAB code via MATLAB's Data Acquisition Toolbox. These signals are then amplified using an off-the-shelf audio amplifier and the amplified signals are supplied to the transducers. The amplifiers are tuned such that the output signal has a peak-to-peak voltage of V_{pp} 14 V. The six phase-shifted signals are generated and supplied to the two unit cells in parallel. The out-of-plane velocity wave field is captured using a Polytech scanning laser Doppler vibrometer (SLDV) using a 1000 500 mm^2 grid with a spatial resolution of 12 points per wavelength and a temporal sampling frequency of 100 kHz. The SLDV is triggered using the custom MATLAB script which generates a 1 ms trigger signal at the start of every measurement to ensure synchronous measurements of all spatial points with the same excitation signal. This enables the reconstruction of the wave field for the time-varying system. The excitation signal is provided for 30 ms and the measurement for each spatial point is conducted for 70 ms to ensure that all the propagating waves present in the elastic domain that were generated during the measurement of the previous point are dampened out and a steady state is achieved before starting the measurement of the following point. Additionally, a 2–4 kHz band-pass filter is applied during post-processing to remove any noise outside the frequency range of interest.

Figure 9 provides the experimental results for the STP phased array with a PT-symmetric phase profile. Specifically, figures 9(a)–(c) show the array's performance during up-converted harmonic suppression, while figures 9(d)–(f) show the performance during down-converted harmonic suppression. The up-converted harmonics are suppressed using modulation depths of 1 35 1 35 . Figure 9(a) displays the experimentally-obtained wave field and shows two transmission channels at the fundamental direction and the first down-converted direction ^{1} , and confirms the negligible propagation in the first up-converted direction ^{1} . To verify the temporal frequency content of the waves traveling in the three principal transmission directions, the spectrum of the signals captured at three marker locations (denoted by green, blue, and red stars on figure 9(a) for the fundamental, up-converted, and down-converted directions, respectively) is plotted in figure 9(b) and is compared with both FE and theoretical predictions, as shown. The suppression of propagations corresponding to the up-converted marker location compared to the two other locations is clearly evident from the three subplots. These plots also serves to confirm that the minimal wave propagation that is seen experimentally along the up-converted direction is predominantly due to cross-talk or side lobes from the other transmission channels, since the highest amplitudes in the rightmost subplot of figure 9(b) correspond to the down-converted and fundamental frequencies as opposed to the suppressed up-converted one. Furthermore, the leftmost subplot of figure 9(b) shows the frequency spectrum of the temporal signal captured along the down-converted direction, and confirms that the first down-converted harmonic ^{1} is dominant in the first down-converted direction ^{1} . This agrees with the theoretical prediction as the modulation depths used in this case align with a full up-converted harmonic suppression with a maximization of the first down-converted harmonic, as discussed in section 4. Finally, figure 9(c) shows the six voltage signals that drive the

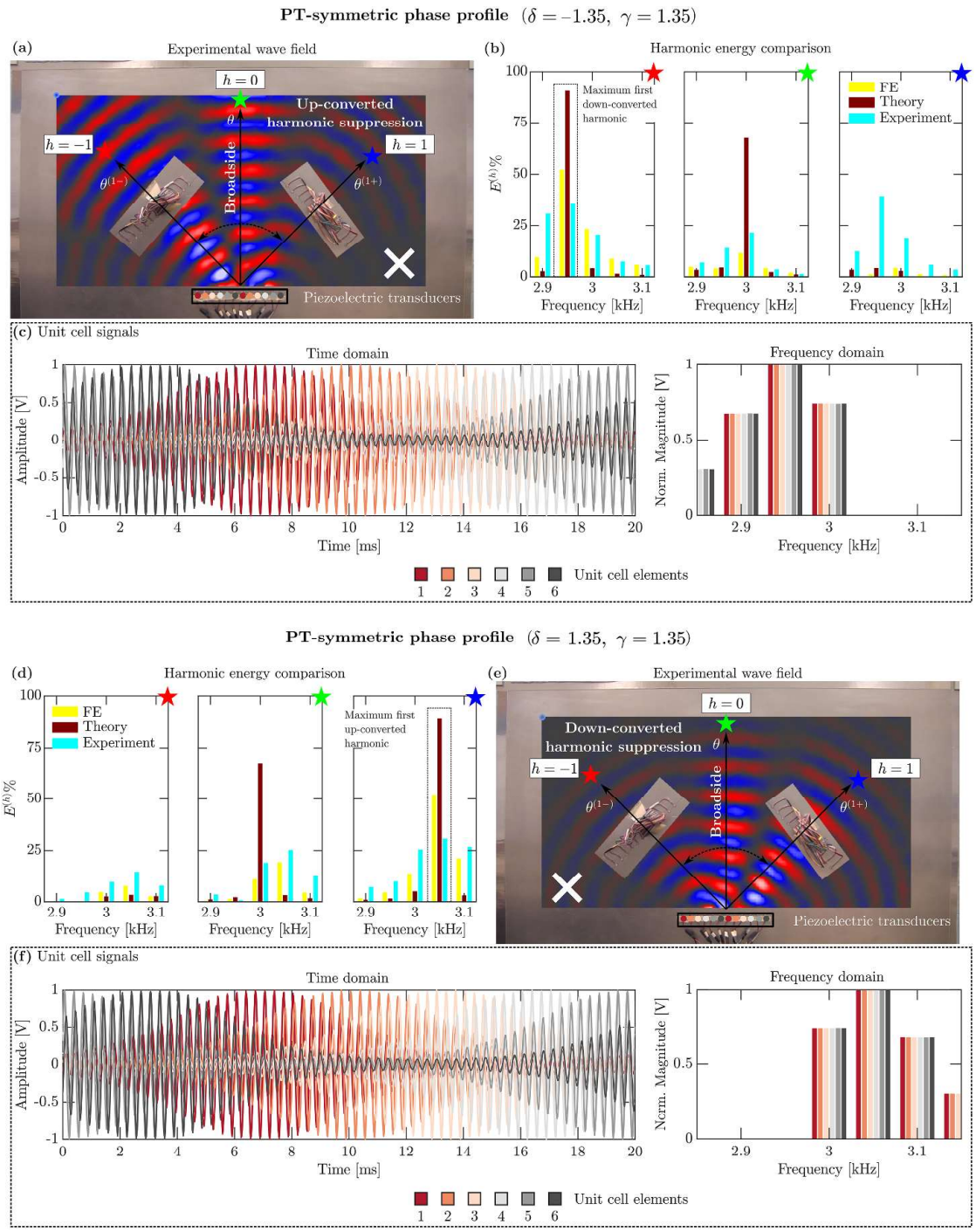

Figure 9. Experiment performance of a non-Hermitian STP elastic phased array with a PT-symmetric phase profile. (a)–(c) show the array's ability to achieve up-converted harmonic suppression at 1 35 1 35 , while maximizing the energy within the first down-converted harmonic. (d)–(f) show the array's ability to achieve down-converted harmonic suppression at 1 35 1 35 , while maximizing the energy within the first up-converted harmonic. (a), (e) show the experimental wave fields, (b), (d) show the frequency spectrum of the signals collected at the three marked locations comparing the experiment to the FE and theoretical predictions, and (c), (f) show the voltage signal sent to the six piezoelectric transducers which constitute a single unit cell of the array in both time and frequency domains.

unit cell in both time and frequency domains. The spatiotemporal variation can be observed in the six signals sent to the unit cell. It is interesting to note that regardless of the different spatiotemporal variations between the six signals, the magnitude of the frequency spectrum remains identical in all six voltage signals as shown in the right column of figure 9(c),

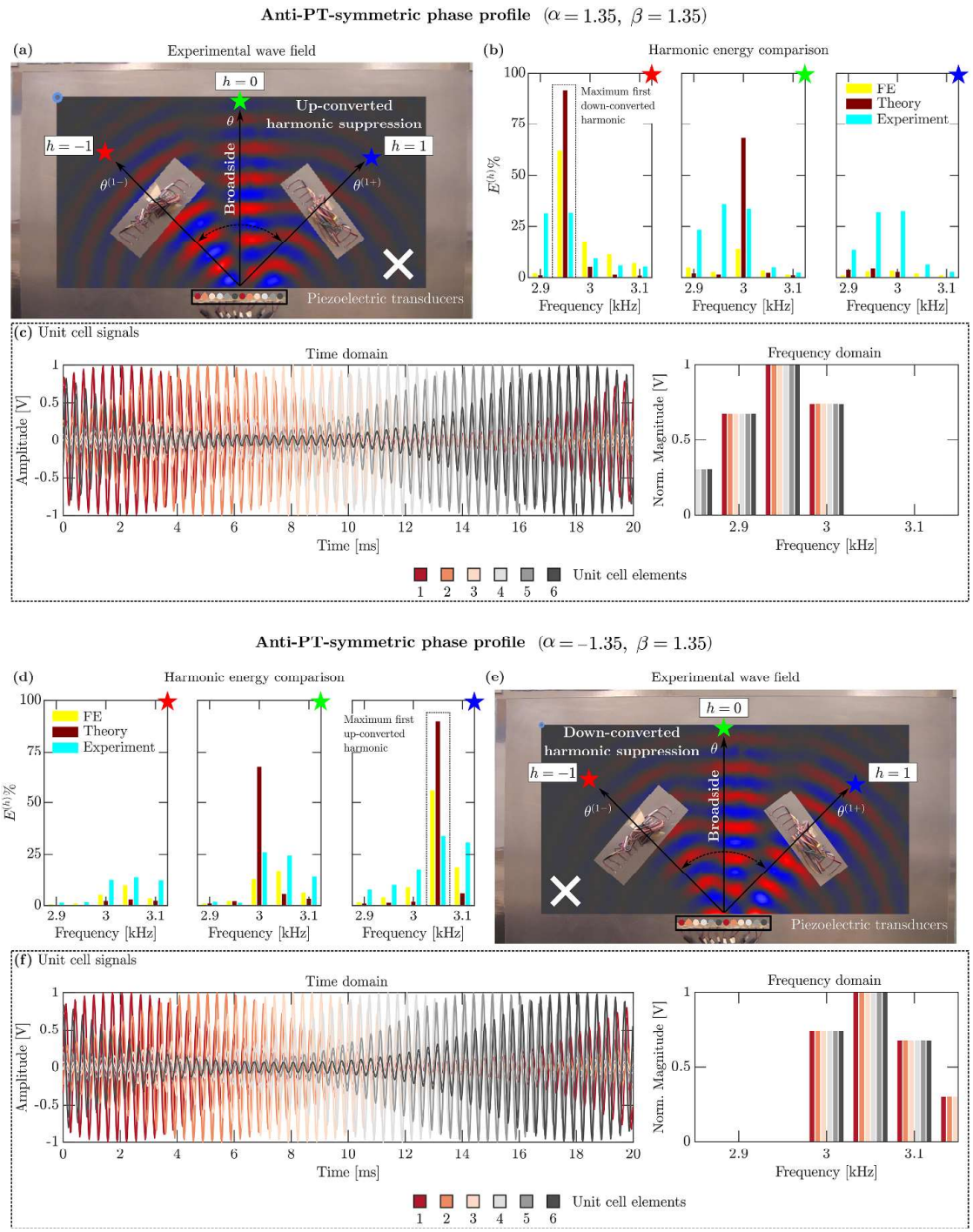

Figure 10. Experiment performance of a non-Hermitian STP elastic phased array with an anti-PT-symmetric phase profile. (a)–(c) show the array's ability to achieve up-converted harmonic suppression at 1 35 1 35 , while maximizing the energy within the first down-converted harmonic. (d)–(f) show the array's ability to achieve down-converted harmonic suppression at 1 35 1 35 , while maximizing the energy within the first up-converted harmonic. (a), (e) show the experimental wave fields, (b), (d) show the frequency spectrum of the signals collected at the three marked locations comparing the experiment to the FE and theoretical predictions, and (c), (f) show the voltage signal sent to the six piezoelectric transducers which constitute a single unit cell of the array in both time and frequency domains.

which shows the suppressed down-converted harmonics and a highest magnitude at the first down-converted frequency, again strongly agreeing with theoretical predictions.

A similar trend is observed in the bottom panel of figure 9 for the down-converted harmonic suppression and maximum first up-converted harmonic case. The optimal modulation

depths used for this case are 1 35 1 35 . The experimentally obtained wave field in figure 9(d) shows the waves propagating in the fundamental and first up-converted direction 1 with negligible energy in the first down-converted direction 1 . Complete suppression of down-converted harmonics is observed on analyzing the frequency spectrum of the captured signals at the three marker locations presented in figure 9(e) with a magnitude peak at the first up-converted frequency 1 . Figure 9(f) shows the voltage signals sent to the unit cell in both time and frequency domains. In the frequency domain, the six voltage signals show the same frequency spectra with the absence of down-converted harmonics and a peak at the first up-converted harmonic.

Akin to the results obtained for the PT-symmetric phase profile, figure 10 displays the experimentally obtained results for the STP phased array with an anti-PT-symmetric phase profile. Particularly, figures 10(a)–(c) show the array's performance during up-converted harmonic suppression while figures 10(d)–(f) show the performance during down-converted harmonic suppression. The up-converted harmonics are suppressed using modulation depths of 1 35 1 35 . Figure 10(a) depicts the experimentally-obtained wave field with two transmission channels at the fundamental direction and the first down-converted direction 1 , and negligible propagation in the first up-converted direction 1 . To verify the temporal frequency content of the waves propagating in the three principal transmission directions, the spectrum of the signals obtained at the three marker locations (denoted by green, blue, and red stars on figure 10(a) for the fundamental, up-converted, and down-converted directions, respectively) are plotted in figure 10(b) and is compared with both FE and theoretical predictions. The suppression of propagations corresponding to the up-converted marker location is evident in the figure. Moreover, the leftmost subplot of figure 10(b) shows the frequency spectrum of the temporal signal obtained along the down-converted direction and confirms the dominance of the first down-converted harmonic 1 in the down-converted direction 1 , agreeing with the theoretical predictions presented in section 4. Lastly, figure 10(c) shows the six voltage signals that drive the unit cell in both time and frequency domains. These show again that irrespective of the different spatiotemporal variations between the six signals, the magnitude of the frequency spectrum remains identical in all six voltage signals as shown in the right column of figure 10(c), showcasing the full suppression of the up-converted harmonics and the maximization of the first down-converted frequency. A similar trend is observed when the modulation depths are set to 1 35 1 35 in order to completely suppress the down-converted harmonics and maximize the first up-converted harmonics, as shown in the bottom panel of figure 10.

Finally, it should be noted that in both PT- and anti-PT-symmetric systems, the input voltage signals contain higher order non-suppressed modes as well. However, due to the choice of parameters for the non-Hermitian phased array, the main lobes generated at higher frequencies (harmonics) are non-propagating modes with a complex transmission angle, but their side lobes remain visible in the other principal directions. Lastly, it is important to reiterate that even though a similar harmonic suppression behavior can be obtained using PT- and anti-PT-symmetric phase profiles (as was shown here), the mechanism by which the behavior is achieved in each case is different.

8. Concluding remarks

In this work, the working concept and underlying physics of a fully operational non-Hermitian STP phased array were presented. Through a comprehensive theoretical analysis backed by experimental testing, it has been shown that the non-Hermitian STP phased array can be tuned to exhibit both PT- and anti-PT-symmetric behaviors by implementing appropriate phase profiles. A theoretical framework was developed to conceptualize and interpret the behavior of both phase profiles in the context of the STP phased array dynamics via an analysis of the eigen spectra by utilizing the scattering matrix. The phase transition from PT (or anti-PT) exact phase to PT (or anti-PT) broken phase was observed in the eigen spectra indicating the presence of EPs, which are characteristic features of PT- and anti-PT-symmetric non-Hermitian systems. On further analysis of the amplitudes of the different harmonics, it was observed that selective suppression of a given set of such harmonics, whether up- or down-converted from the fundamental frequency, can be achieved at the EPs. Additionally, an optimization problem was formulated to maximize the energy contained within a specific non-suppressed mode at the EPs. Expressions for the wave field generated by the non-Hermitian STP phased array were derived and used to predict the principal propagation directions corresponding to the non-suppressed modes, and full-wave FE numerical simulations were utilized to validate the theoretical results. Finally, an experimental realization of the non-Hermitian array was developed and tested in order to verify the feasibility of the on-demand harmonic suppression scheme presented earlier. The results presented here can be the foundation of a new class of adaptive phased arrays which can robustly and efficiently achieve 'on-the-fly' directional wave beaming with unprecedented control over transmission directions and energy levels contained therein. In the mechanical domains, non-Hermitian STP phased arrays have the potential to advance acoustic communication systems given their ability to communicate with multiple carriers at different frequencies, while simultaneously modulating the amplitude of specific directional channels. This can be easily tailored to ensure appropriate communication strength or compensate for carriers at different proximity levels. They can similarly impact a wide range of applications ranging from sensing and communication to SONAR/RADAR, object detection, focusing, and source localization. Moreover, by invoking multiple non-Hermitian STP arrays, the proposed system can triangulate multiple objects by augmenting traditional time-delay methods with amplitude information of the incident signals from different directional channels. As a result, these systems can be extended to 5G communication and internet connectivity through constellation systems such as Starlink.

Data availability statement

All data that support the findings of this study are included within the article (and any supplementary files).

Acknowledgments

The authors acknowledge the support of this work from the US National Science Foundation through Awards No. 1847254 (CAREER) and 1904254.

ORCID iDs

R Adlakha https://orcid.org/0000-0002-0414-8948
M Nouh https://orcid.org/0000-0002-2135-5391

References

[1] Palmer R *et al* 2022 A primer on phased array radar technology for the atmospheric sciences *Bull. Am. Meteorol. Soc.* **103** E2391–416
[2] Huang G, Benesty J, Cohen I and Chen J 2020 A simple theory and new method of differential beamforming with uniform linear microphone arrays *IEEE/ACM Trans. Audio Speech Lang. Process.* **28** 1079–93
[3] Marzo A, Ann Seah S, Drinkwater B W, Ranjan Sahoo D, Long B and Subramanian S 2015 Holographic acoustic elements for manipulation of levitated objects *Nat. Commun.* **6** 1–7
[4] Marzo A, Barnes A and Drinkwater B W 2017 Tinylev: a multi-emitter single-axis acoustic levitator *Rev. Sci. Instrum.* **88** 085105
[5] Kumar B P and Branner G R 2005 Generalized analytical technique for the synthesis of unequally spaced arrays with linear, planar, cylindrical or spherical geometry *IEEE Trans. Antennas Propag.* **53** 621–34
[6] Hassanien A and Vorobyov S A 2010 Phased-mimo radar: a tradeoff between phased-array and mimo radars *IEEE Trans. Signal Process.* **58** 3137–51
[7] Sadhu B *et al* 2017 7.2 a 28ghz 32-element phased-array transceiver ic with concurrent dual polarized beams and 1.4 degree beam-steering resolution for 5g communication *2017 IEEE Int. Solid-State Circuits Conf. (ISSCC)* (IEEE) pp 128–9
[8] Zhang J, Zhang S, Lin X, Fan Y and Frølund Pedersen G 2018 3d radiation pattern reconfigurable phased array for transmission angle sensing in 5g mobile communication *Sensors* **18** 4204
[9] Kibaroglu K, Sayginer M and Rebeiz G M 2018 A low-cost scalable 32-element 28-ghz phased array transceiver for 5g communication links based on a 2 2 beamformer flip-chip unit cell *IEEE J. Solid-State Circuits* **53** 1260–74
[10] Hawksford M O J 2011 Hrtf-enabled microphone array for binaural synthesis *Audio Engineering Society Convention 130* (Audio Engineering Society) p 8391
[11] Hamdan E C and Maria Fazi F 2021 Weighted orthogonal vector rejection method for loudspeaker-based binaural audio reproduction *IEEE/ACM Trans. Audio Speech Lang. Process.* **29** 1844–52
[12] Hamdan E C and Maria Fazi F 2021 Ideal focusing and optimally-conditioned systems in sound field control with loudspeaker arrays *J. Sound Vib.* **509** 116218
[13] Simón Gálvez M F, Elliott S J and Cheer J 2014 Personal audio loudspeaker array as a complementary tv sound system for the hard of hearing *IEICE Trans. Fundam. Electron. Commun. Comput. Sci.* **97** 1824–31
[14] Simón Gálvez M F, Menzies D and Maria Fazi F 2019 Dynamic audio reproduction with linear loudspeaker arrays *J. Audio Eng. Soc.* **67** 190–200
[15] Ohara Y, Yamamoto S, Mihara T and Yamanaka K 2008 Ultrasonic evaluation of closed cracks using subharmonic phased array *Jpn. J. Appl. Phys.* **47** 3908
[16] Kazari H, Kabir M, Mostavi A and Ozevin D 2019 Multi-frequency piezoelectric micromachined ultrasonic transducers *IEEE Sens. J.* **19** 11090–9
[17] Lingyu L and Giurgiutiu V 2007 In-situ optimized pwas phased arrays for lamb wave structural health monitoring *J. Mech. Mater. Struct.* **2** 459–87
[18] Giurgiutiu V and Bao J 2004 Embedded-ultrasonics structural radar for in situ structural health monitoring of thin-wall structures *Struct. Health Monit.* **3** 121–40
[19] Lingyu L and Giurgiutiu V 2008 In situ 2-d piezoelectric wafer active sensors arrays for guided wave damage detection *Ultrasonics* **48** 117–34
[20] Zhang X, Zhou W, Li H and Zhang Y 2020 Guided wave-based bend detection in pipes using in-plane shear piezoelectric wafers *NDT&E Int.* **116** 102312
[21] Vahedi M, Ardestani R and Mehdi Zahrai S M 2021 Sensitivity analysis of tubular-web reduced beam section connections under cyclic loading *Int. J. Steel Struct.* **21** 100–17
[22] Momeni H and Ebrahimkhanlou A 2022 High-dimensional data analytics in structural health monitoring and non-destructive evaluation: a review paper *Smart Mater. Struct.* **31** 043001
[23] Wang W, Zhang H, Lynch J P, Cesnik C E S and Li H 2018 Experimental and numerical validation of guided wave phased arrays integrated within standard data acquisition systems for structural health monitoring *Struct. Control Health Monit.* **25** e2171
[24] Salas K I and Cesnik C E S 2009 Guided wave excitation by a clover transducer for structural health monitoring: theory and experiments *Smart Mater. Struct.* **18** 075005
[25] Polychronopoulos S and Memoli G 2020 Acoustic levitation with optimized reflective metamaterials *Sci. Rep.* **10** 4254
[26] Cox L, Melde K, Croxford A, Fischer P and Drinkwater B W 2019 Acoustic hologram enhanced phased arrays for ultrasonic particle manipulation *Phys. Rev. Appl.* **12** 064055
[27] Adlakha R, Moghaddaszadeh M, Attarzadeh M A, Aref A and Nouh M 2020 Frequency selective wave beaming in nonreciprocal acoustic phased arrays *Sci. Rep.* **10** 1–14
[28] Adlakha R, Moghaddaszadeh M, Attarzadeh M A, Aref A and Nouh M 2020 A linear acoustic phased array for nonreciprocal transmission and reception *ASME Int. Mechanical Engineering Congress and Exposition* vol 84478 (American Society of Mechanical Engineers) p V001T01A016
[29] Moghaddaszadeh M, Adlakha R, Attarzadeh M A, Aref A and Nouh M 2021 Nonreciprocal elastic wave beaming in dynamic phased arrays *Phys. Rev. Appl.* **16** 034033
[30] Bender C M and Boettcher S 1998 Real spectra in non-hermitian hamiltonians having p t symmetry *Phys. Rev. Lett.* **80** 5243
[31] Longhi S 2015 Half-spectral unidirectional invisibility in non-hermitian periodic optical structures *Opt. Lett.* **40** 5694–7
[32] McDonald A and Clerk A A 2020 Exponentially-enhanced quantum sensing with non-hermitian lattice dynamics *Nat. Commun.* **11** 1–12
[33] Fang X, Gerard N J R K, Zhou Z, Ding H, Wang N, Jia B, Deng Y, Wang X, Jing Y and Li Y 2021 Observation of higher-order exceptional points in a non-local acoustic metagrating *Commun. Phys.* **4** 1–7

[34] Wang W, Wang L-Q, Xue R-D, Chen H-L, Guo R-P, Liu Y and Chen J 2017 Unidirectional excitation of radiative-loss-free surface plasmon polaritons in p t-symmetric systems *Phys. Rev. Lett.* **119** 077401
[35] Zhao B, Sun L-S and Chen J 2020 Hybrid parity-time modulation phase and geometric phase in metasurfaces *Opt. Express* **28** 28896–905
[36] Kawaguchi Y, Alu A and Khanikaev A B 2022 Non-reciprocal parity-time symmetry breaking based on magneto-optical and gain/loss double ring resonators *Opt. Mater. Express* **12** 1453–60
[37] Riva E 2022 Harnessing pt-symmetry in non-hermitian stiffness-modulated waveguides *Phys. Rev.* B **105** 224314
[38] Moghaddaszadeh M, Attarzadeh M A, Aref A and Nouh M 2022 Complex spatiotemporal modulations and non-hermitian degeneracies in p t-symmetric phononic materials *Phys. Rev. Appl.* **18** 044013
[39] Ge L and Türeci H E 2013 Antisymmetric pt-photonic structures with balanced positive-and negative-index materials *Phys. Rev.* A **88** 053810
[40] Yang F, Liu Y-C and You Li 2017 Anti-pt symmetry in dissipatively coupled optical systems *Phys. Rev.* A **96** 053845
[41] Fan H, Chen J, Zhao Z, Wen J and Huang Y-P 2020 Antiparity-time symmetry in passive nanophotonics *ACS Photon.* **7** 3035–41
[42] Zhang F, Feng Y, Chen X, Ge Li and Wan W 2020 Synthetic anti-pt symmetry in a single microcavity *Phys. Rev. Lett.* **124** 053901
[43] Miri M-A and Alu A 2019 Exceptional points in optics and photonics *Science* **363** eaar7709
[44] Zhang G-Li, Liu Di and Yung M-H 2021 Observation of exceptional point in a pt broken non-hermitian system simulated using a quantum circuit *Sci. Rep.* **11** 1–8
[45] Xia S, Danieli C, Zhang Y, Zhao X, Lu H, Tang L, Li D, Song D and Chen Z 2021 Higher-order exceptional point and landau–zener bloch oscillations in driven non-hermitian photonic lieb lattices *APL Photon.* **6** 126106
[46] Giurgiutiu V 2007 *Structural Health Monitoring: With Piezoelectric Wafer Active Sensors* (Amsterdam: Elsevier)
[47] Pant S, Laliberte J and Martinez M 2013 Structural health monitoring (shm) of composite aerospace structures using lamb waves *Proc. 19th Int. Conf. on Composite Materials* (*Montreal, QC, Canada*) vol 28